Bioactive Materials 41 (2024) 96–107

Contents lists available at ScienceDirect

Bioactive Materials

journal homepage: www.keaipublishing.com/en/journals/bioactive-materials

Degradation behavior of austenite, ferrite, and martensite present in biodegradable Fe-based alloys in three protein-rich pseudo-physiological solutions

Abdelhakim Cherqaoui [a], Quang Nguyen Cao [a], Maria Laura Gatto [b], Carlo Paternoster [a], Paolo Mengucci [c], Diego Mantovani [a,*]

[a] Laboratory for Biomaterials and Bioengineering, Canada Research Chair I in Biomaterials and Bioengineering for the Innovation in Surgery, Department of Min-Met-Materials Engineering, Research Center of CHU de Quebec, Division of Regenerative Medicine, Laval University, Quebec City, Canada
[b] Department DIISM, Università Politecnica Delle Marche, Via Brecce Bianche 12, 60131, Ancona, Italy
[c] Department SIMAU & UdR INSTM, Università Politecnica Delle Marche, Via Brecce Bianche 12, 60131, Ancona, Italy

ARTICLE INFO

Keywords:
Biodegradable metals
Fe-based alloys
Degradation
Albumin
Pseudo-physiological solutions

ABSTRACT

This study investigates the degradation behavior of three distinct Fe-based alloys immersed in three pseudo-physiological solutions. These alloys, which have varied Mn and C contents, include a commercially available Fe-0.15C alloy, namely Fe–C, and two newly developed alloys, that is Fe–5Mn-0.2C (namely Fe–5Mn) and Fe–18Mn-0.6C (namely Fe–18Mn). The aim was to understand the effect of alloying elements and the testing solution on the *in-vitro* degradation behavior of these Fe-based materials. Static immersion degradation and potentiodynamic corrosion tests were carried out using three pseudo-physiological solutions with albumin supply, that is modified Hanks' saline solution (MHSS), phosphate buffered saline solution (PBS), and sodium chloride solution (NaCl). After two weeks of static immersion, the results revealed that Fe–5Mn, characterized by a mixture of ferrite and martensite, showed the highest degradation rate, while Fe–C, composed solely of ferrite, showed the lowest rate of degradation. The predominant degradation products in MHSS and PBS were phosphates and carbonates. In PBS, these products formed a remarkably stable protective layer on the surface, contributing to the lowest degradation rate. In contrast, porous hydroxides appeared as the main degradation products for samples immersed in NaCl solution, leading to the highest degradation rate. These results provided important insights into the customization of Fe–Mn–C alloys for a range of biomedical applications, meeting a variety of clinical requirements, and highlighting the considerable potential of Fe–Mn–C alloys for biomedical applications.

1. Introduction

Fe-based alloys are potential candidates for biodegradable implant applications, such as bioabsorbable stents, due to their excellent mechanical properties and biocompatibility [1–3]. However, the slow degradation of these alloys in physiological environments hindered their practical applications so far [4]. For example, *Peuster* et al. [5] observed that considerable portions of a pure Fe stent implanted in a porcine descending aorta remained largely intact even after twelve months. Therefore, research into biodegradable Fe-based alloys focused on exploring new approaches to accelerate their degradation; in this context, the use of physiological or pseudo-physiological environments has always considered fundamental to understand preliminarily the material degradation patterns and kinetics.

Several strategies have been proposed to address this crucial issue related to biodegradable Fe-based alloys. These include alloying element incorporation [6–8], microstructure tuning [7–10], introduction of secondary phases [9–11], and the use of 3D printing as a manufacturing process [12–14]. Among these strategies, the addition of Mn and C as alloying elements is particularly promising. Fe–Mn–C alloys have shown

Peer review under responsibility of KeAi Communications Co., Ltd.
* Corresponding author.
E-mail addresses: abdelhakim.cherqaoui.1@ulaval.ca (A. Cherqaoui), nguyen.cao-quang.1@ulaval.ca (Q.N. Cao), m.l.gatto@staff.univpm.it (M.L. Gatto), carlo.paternoster.1@ulaval.ca (C. Paternoster), p.mengucci@staff.univpm.it (P. Mengucci), Diego.mantovani@gmn.ulaval.ca (D. Mantovani).

https://doi.org/10.1016/j.bioactmat.2024.06.025
Received 28 January 2024; Received in revised form 1 June 2024; Accepted 16 June 2024
Available online 16 July 2024

exceptional mechanical properties and accelerated initial biodegradation rates [15–18]. Mn plays an important role in improving both the mechanical properties and degradation rate (DR) of Fe-based alloys. In addition, Mn and C are largely considered biodegradable and biocompatible alloying elements [19]. In this regard, *Mouzou* et al. [15] and *Gambaro* et al. [16] have used Mn and C as alloying elements to develop four different Fe–Mn–C alloys, which exhibited impressive mechanical properties with tensile strength reaching up to 1230 MPa and elongation exceeding 50 %. Static immersion tests carried out in a MHSS revealed an accelerated initial DR compared with pure Fe. However, the formation of carbonates or phosphates during the degradation process prevented complete degradation. *Conti* et al. [17] employed cold rolling to enhance the tensile strength of a Fe–13Mn-1.2C alloy to around 1300 MPa and examined its degradation behavior in Hanks' solution, with and without the presence of albumin. The results of 2 weeks of static immersion tests revealed that the formation of $MnCO_3$ and $FeCO_3$ as the main degradation products (DPs) facilitated the development of a stable protective layer over the surface, leading to an exceptionally low DR of approximately DR = 0.006 mm/year. In a recent study, *Loffredo* et al. [18] introduced 0.4 wt % Ag into Fe–16Mn-0.7C intending to accelerate the DR while preserving the mechanical properties of the alloy for use in biodegradable stent applications. Nevertheless, the static immersion test results indicate that the formation of a passive and stable layer after one month of immersion hindered subsequent degradation processes. In conclusion, most of the recent studies on Fe–Mn–C alloys showed the formation of carbonates/phosphates as the main DPs on the surface of the substrates. These DPs were also shown to act as a stable protective layer resulting in a lower degradation rate, and inhibiting full rapid biodegradation. This critical issue represents the bottleneck that hinders Fe–Mn–C alloys from further advancement toward clinical translation.

To address this major challenge, it is essential to understand the impact of existing phases on the degradation behavior of Fe–Mn–C alloys. Therefore, this study aims to explore the degradation behavior of the different metallurgical phases present in three different Fe-based alloys. Fe–18Mn-0.6C (Fe–18Mn), Fe–5Mn-0.2C (Fe–5Mn), and commercial Fe–C alloys were chosen based on Schumann's diagram [20]. The Fe–C alloy consists only of ferrite, while Fe–5Mn has a dual-phase structure of ferrite (or α-Fe) and martensite (or α′-Fe), and Fe–18Mn is composed completely of austenite (or γ-Fe). It should be noted that the majority of the previous investigations documented in the literature concerning Fe–Mn–C alloys contained Mn concentrations above 12 wt%, comprising mainly austenite alone, with traces of martensite [15–18]. This work comprehensively studied the effect of three different solutions on the degradation of the ferrite, martensite, and austenite phases in the selected alloys. Static immersion degradation and potentiodynamic polarization tests were carried out in the three most common pseudo-physiological solutions, like MHSS, PBS, and NaCl, to assess the degradation behavior of Fe–Mn–C alloys in these environments. Albumin was added to all three solutions due to its prominence as the most abundant protein in human blood [21].

2. Materials and methods

2.1. Samples preparation and chemical composition

Fe–5Mn and Fe–18Mn alloys were newly designed and cast from pure elements (Fe > 99.9 %, Mn > 99.7 %, and C > 99.9 %), while AISI1018 was obtained from a commercial provider (McMaster -Carr). The casting process, for Fe–5Mn and Fe–18Mn, took place in an induction melting furnace equipped with a liquid argon protection system. The cast alloys then underwent a solution heat treatment at 1100 °C for 12 h in a vacuum furnace, to prevent decarburization. The three alloys were then hot and cold rolled to a thickness of 1 mm. Specimens measuring 20 mm × 10 mm x 1 mm were then cut from each alloy sheet and polished using SiC abrasive papers up to a grit size of 800. Successively, fine polishing was performed using 6 μm, 3 μm, and 1 μm diamond paste, followed by rinsing with ethanol and air drying. The mechanically polished samples, for all the alloys, were considered as the reference condition (namely "as-received").

The experimental chemical composition of the as-received alloys is shown in Table 1. The quantification of Fe and Mn (wt.%) amounts of as-received samples was carried out by microwave plasma atomic emission spectroscopy (MP-AES) using an Agilent Technologies 4100^{+} MP-AES (4100 upgraded to a 4200-torch system), while the amount of C (wt. %) was analyzed by a pyrolytic carbon/sulfur detector (LECO CS200).

2.2. Microstructural and chemical characterization

The microstructure of the etched (Nital 2 %) as-received samples was analyzed using a FEI Quanta 250 scanning electron microscope (SEM), which was equipped with an EDAX-Amatec energy-dispersive microanalysis (EDS) system. The average grain size of the three alloys was determined from SEM micrographs at a 20 μm scale following the ASTM E112 standard [22] using ImageJ software. Furthermore, SEM was utilized to observe the surface morphology of at least three specimens for each condition, before and after static immersion degradation tests, and for the analysis of their corresponding degradation products (DPs). The chemical composition of these degraded surfaces and the associated DPs were determined through EDS microanalysis.

X-ray diffraction (XRD) was employed to gather information on the crystallographic structure of the sintered samples. The analysis was carried out using a Bruker D8 Advance diffractometer with $Cu_{K\alpha}$ ($\lambda_{CuK\alpha}$ = 1.5406 Å) radiation, equipped with a monochromator and operating at V = 40 kV and I = 40 mA within an angular range of 2θ = 20°–80°. The DIFFRAC.EVA software package has been used to analyze the obtained XRD patterns, while peak indexing was achieved through the search/match facility using the PDF 2 database of the International Center for Diffraction Data (ICDD).

The DPs were identified using attenuated total reflectance Fourier transform infrared spectroscopy (FTIR). The equipment used for this analysis was an Agilent Cary 660 FTIR instrument (Agilent Technologies, MN, USA). FTIR acquisition covered the wavelength range of 4000-400 cm^{-1} with a resolution of 4 cm^{-1}.

2.3. Degradation behavior

2.3.1. Pseudo-physiological solutions preparation

Three different pseudo-physiological solutions (MHSS, PBS, NaCl) were used for static immersion degradation tests and potentiodynamic polarization (PDP) analyses on the as-received samples. Each solution was supplemented with 2 g/L of albumin to closely mimic the composition of blood plasma. The specific salt concentrations and ionic compositions of these solutions are detailed in Table 2. Furthermore, the pH of these albumin-supplemented solutions (MHSS, PBS, and NaCl) was adjusted to 7.4 by the addition of 1 M HCl or NaOH solutions.

2.3.2. Static immersion degradation tests

The static immersion degradation tests were conducted on the as-received samples of the three chosen Fe–C-based alloys, following the ASTM G31-03 standard [23]. Before the immersion tests, all specimens were weighed using a 5-digit precision digital balance (Analytical Plus, Ohaus, USA). Five samples for each alloy were then immersed in the three albumin-supplemented solutions. The samples were suspended

Table 1
Chemical composition of Fe–C, Fe–5Mn, and Fe–18Mn as-received samples.

As-received sample	Chemical elements (wt.%)		
	Fe	Mn	C
Fe–C	Bal.	0.73 ± 0.02	0.15 ± 0.01
Fe–5Mn	Bal.	4.64 ± 0.08	0.22 ± 0.01
Fe–18Mn	Bal.	17.68 ± 0.12	0.66 ± 0.02

Table 2
Salt concentration of albumin-supplemented pseudo-physiological solutions used for the static immersion degradation and PDP tests.

Reference name	The salt concentration of the three solutions					
	Deionized water	Salts	HEPES acid	HEPES Na salt	$NaHCO_3$	Bovine serum albumin
MHSS	1.4 L	9.7 g of Hanks' balanced salts	14.16 g	16.65 g	3.3 g	2.8 g
PBS	1 L	9.6 g of Dulbecco's phosphate-buffered saline	–	–	–	2 g
NaCl	1 L	8.94 g of NaCl	–	–	–	2 g

using a nylon thread in covered and loosely-capped beakers containing 90 mL of solution. After being immersed for 14 days in an incubator set at 37.0 ± 1 °C, with p_{CO2} = 5 vol% and relative humidity RH = 90 %, the samples were removed and subjected to ultrasonic cleaning for 5 min in 20 mL of a 70 vol% ethanol solution. Following cleaning, each sample was reweighed. Subsequently, the degraded surfaces were characterized using SEM/EDS analysis, as described in paragraph 2.2. The solution used for the cleaning procedure, rich in degradation products detached from the extracted samples, was also collected and treated in the same way as the waste solution described below.

The waste solution from the static immersion degradation tests was collected and centrifuged at ν = 3000 rpm for 10 min to separate the supernatant from the precipitated DPs. The supernatant was disposed of, while the sedimented particles (DPs) were then mixed with a solution consisting of 50 vol% pure ethanol and 50 vol% deionized water (washing); they were subjected to vortexing, centrifuged, and again washed. The resulting DPs were collected and desiccated at 37 °C under a pressure of 30 Torr before undergoing further analysis via SEM/EDS and FTIR, as outlined in paragraph 2.2.

The degradation rate (DR) of samples was calculated following Equation (1), according to ASTM G31-03 [23]:

$$DR = 8.76 \cdot 10^4 \frac{W}{A \cdot t \cdot \rho} \quad (1)$$

Where DR is the degradation rate (mm/year), W is the mass loss (g), calculated as the difference between the sample weight before and after the immersion test, A is the area of the sample (cm^2), t is immersion time (h) and ρ is the material density (g/cm^3). Values of degradation rate (DR) of Fe–Mn, Fe–5Mn, and Fe–18Mn samples after static immersion degradative tests in MHSS, PBS, and NaCl, were presented as mean ± standard deviation.

2.3.3. Potentiodynamic polarization tests

PDP tests were conducted according to the ASTM G59-97 standard [24] using samples measuring 10 mm × 10 mm x 1 mm. A three-electrode cell setup, using a VersaSTAT3 potentiostat/galvanostat system from Princeton Applied Research, USA, was utilized for these tests. This setup included a saturated calomel reference electrode, graphite rods serving as counter electrodes, and the sample itself acting as the working electrode [25]. At least three samples for each alloy were tested in the albumin-supplemented pseudo-physiological solutions.

Before the PDP tests, the stabilization of open circuit potential (OCP) was monitored for 1 h. The PDP tests were carried out at a scan rate of 0.166 mV/s, covering a potential range from −0.35 V to 1 V versus OCP, with a voltage step of 1 mV and a time step of 6 s. The corrosion rate (CR) was calculated using Equation (2), based on the ASTM G59 standard [24]:

$$CR = 3.27 \cdot 10^{-3} \frac{i_{corr}\, EW}{\rho} \quad (2)$$

Where CR is the corrosion rate (mm/year), i_{corr} is the current density ($\mu A \cdot cm^{-2}$), ρ is the sample density ($g \cdot cm^{-3}$) and EW is the equivalent weight. For an alloy, the EW is calculated in the following Equation (3):

$$EW = \frac{1}{\sum_i \frac{n_i f_i}{W_i}} \quad (3)$$

Where f_i is the mass fraction of the ith element in the alloy, W_i is the atomic weight of the ith element in the alloy (W_{Fe} = 55.845 a. m. u., W_{Mn} = 54.938 a. m. u.), and n_i is the valence of the ith element of the alloy; C s not considered because of its small amount.

3. Results

3.1. Structural characterization

XRD patterns of Fe–C, Fe–5Mn, and Fe–18Mn as-received conditions are reported in Fig. 1. To facilitate comparison, the patterns in Fig. 1 were vertically adjusted. Peaks revealed the presence of α-Fe (ferrite) body-centered cubic (bcc) phase (ICDD 6–696) with a nominal lattice parameter a = 0.28664 nm for Fe–C and Fe–5Mn. Contrarily, Fe–18Mn showed the presence of austenite, with a face-centered cubic microstructure (ICDD 33–397), and a nominal lattice parameter a = 0.35911 nm. In the case of Fe–5Mn, a peak corresponding to martensite was detected at 64.7°, which was closely aligned with the ferrite peak at 64.9°. These results, namely the presence of ferrite in Fe–C, ferrite and martensite in Fe–5Mn, and austenite in Fe–18Mn agreed with Schumann's diagram [20].

SEM examinations of the microstructures of the as-received samples in Fe–C, Fe–5Mn, and Fe–18Mn are presented in Fig. 2. Additionally, Table 3 summarizes the calculated phase compositions and average grain sizes of each alloy. In Fe–C, a uniform microstructure predominated, composed mainly of small equiaxial ferrite grains with an average size of approximately 5 μm. Conversely, Fe–5Mn exhibits a dual-phase microstructure comprised of martensite and ferrite, with an average grain size of around 7 μm. Rietveld analysis conducted on this alloy confirms the presence of ferrite (bcc or α-Fe) with a calculated lattice parameter of a = 0.286835 and martensite (tetragonal or α′-Fe) with calculated lattice parameters of a = 0.286835 and c = 0.287370. This low tetragonality martensite has been previously reported in the literature for alloys with similar chemical compositions [26–31].

Finally, Fe–18Mn presents a non-equiaxial microstructure,

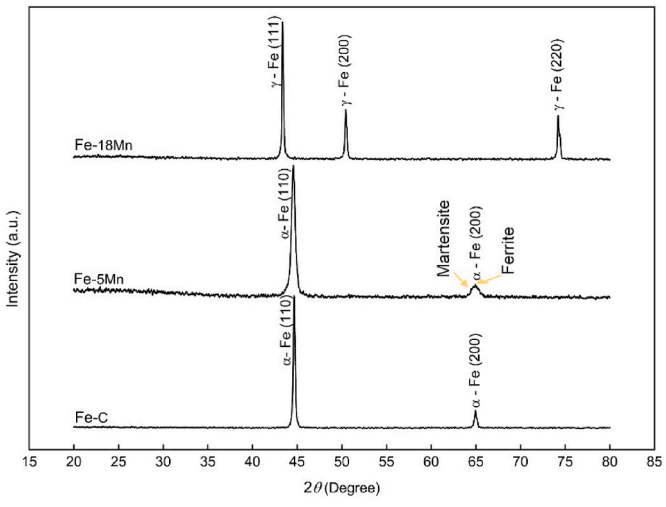

Fig. 1. XRD patterns of Fe–C, Fe–5Mn, and Fe–18Mn as-received samples.

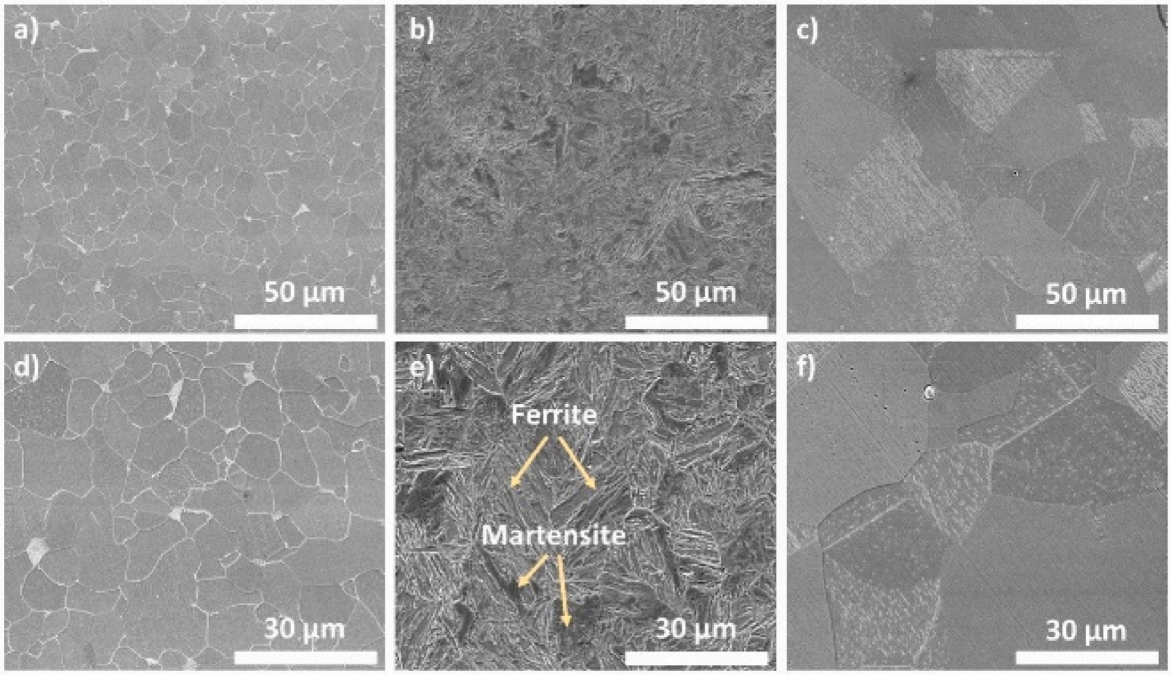

Fig. 2. SEM micrographs: a) Fe–C (a, d); Fe–5Mn (b, e); Fe–18Mn (c, f) as-received samples.

Table 3
Phase composition and average grain size of Fe–C, Fe–5Mn, and Fe–18Mn as-received samples.

	Weight fraction of different phases (wt.%)			Average grain size (µm)
	α-Fe	γ-Fe	α′-Fe	
Fe–C	100	–	–	5.10 ± 0.89
Fe–5Mn	73	–	27 ± 9	7.03 ± 0.96
Fe–18Mn	–	100	–	19.71 ± 1.71

illustrated at lower magnification in Fig. 2c, with an average grain size of about 20 µm.

3.2. Static immersion degradation tests

DRs of the investigated alloys, following static immersion degradation tests for 14 days in the three pseudo-physiological solutions are plotted in Fig. 3. Notably, NaCl resulted in the highest DRs; PBS was on the opposite end of the spectrum, showing in general a very low DR. Generally, Fe–5Mn exhibited the highest DRs for all three solutions. Specifically, for MHSS immersion, DRs were $DR_{Fe\text{-}C,\ HMSS} = 0.09 \pm 0.009$ mm/year for Fe–C alloy, $DR_{Fe\text{-}5Mn,\ HMSS} = 0.195 \pm 0.026$ mm/year for Fe–5Mn alloy, and $DR_{Fe\text{-}18Mn,\ HMSS} = 0.08 \pm 0.005$ mm/year for Fe–18Mn alloy. As anticipated, all three alloys showed very low DRs in PBS solution, approximately 0.030 ± 0.004 mm/year. Contrarily, the highest DRs occurred in the NaCl solution, reaching $DR_{Fe\text{-}C,\ NaCl} = 0.220 \pm 0.016$ mm/year for Fe–C, $DR_{Fe\text{-}5Mn,\ NaCl} = 0.274 \pm 0.011$ mm/year for Fe–5Mn, and $DR_{Fe\text{-}18Mn,\ NaCl} = 0.217 \pm 0.023$ mm/year for Fe–18Mn.

The morphology and EDS analysis of the degraded surfaces of the immersed alloys are presented in Fig. 4. Some residual DPs were observed on the degraded surfaces. Examination of these remaining DPs revealed a consistent structure for all the considered media. For MHSS, two distinct sub-layers of DPs were identified. EDS analysis, with three representative specimens of Fe–18Mn, each one immersed in one of the three considered media, are shown in Fig. 4 (c,f, and i). The corresponding EDS highlighted three points that were related to the different layers formed by the degradation products: point 1 corresponded to the top layer, point 2 to the intermediate one, and point 3 to the substrate

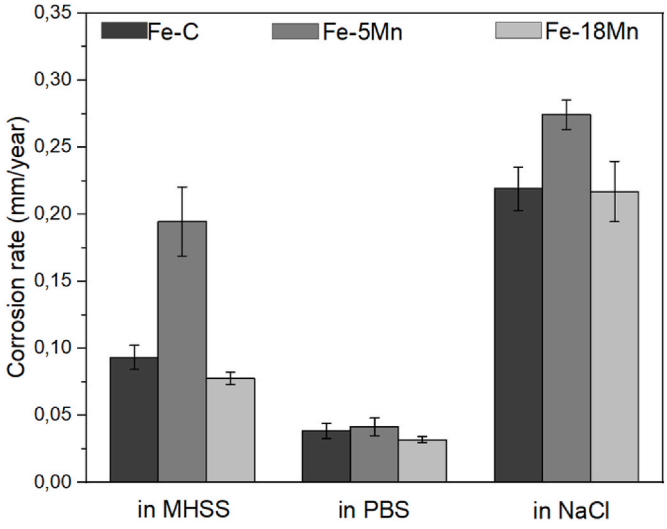

Fig. 3. Degradation rates of Fe–C, Fe–5Mn, and Fe–18Mn alloys after 14 days of static immersion degradation test in MHSS, PBS, and NaCl solutions.

(Fig. 4c). The top layer predominantly consisted of P, O, C, and Ca; this could be associated to the presence of oxides, phosphates, and carbonates, as described by other authors. The presence of $Ca_2P_2O_7$ was also confirmed by XRD (Fig. 5). Meanwhile, the intermediate layer was primarily composed of Fe, O, Mn, and C, compatible with the presence of hydroxides and carbonates. Fe/Mn carbonates ($(Fe, Mn)CO_3$) were observed within the DPs of all the samples immersed in MHSS (Fig. 6j), which was consistent with prior research findings [16,25]. In PBS solution, a similar two sub-layer structure of DPs was observed (Fig. 4f). The inner sub-layer exhibited a thin solid structure primarily composed of phosphates/carbonates with traces of Cl, while the inner sub-layer resembled the hydroxide composition observed in the intermediate layer of the samples immersed in MHSS (Fig. 4k). Contrarily, in NaCl-immersed samples, the outer layer of DPs detached from the degraded surfaces, leaving behind remnants of the inner layer. EDS

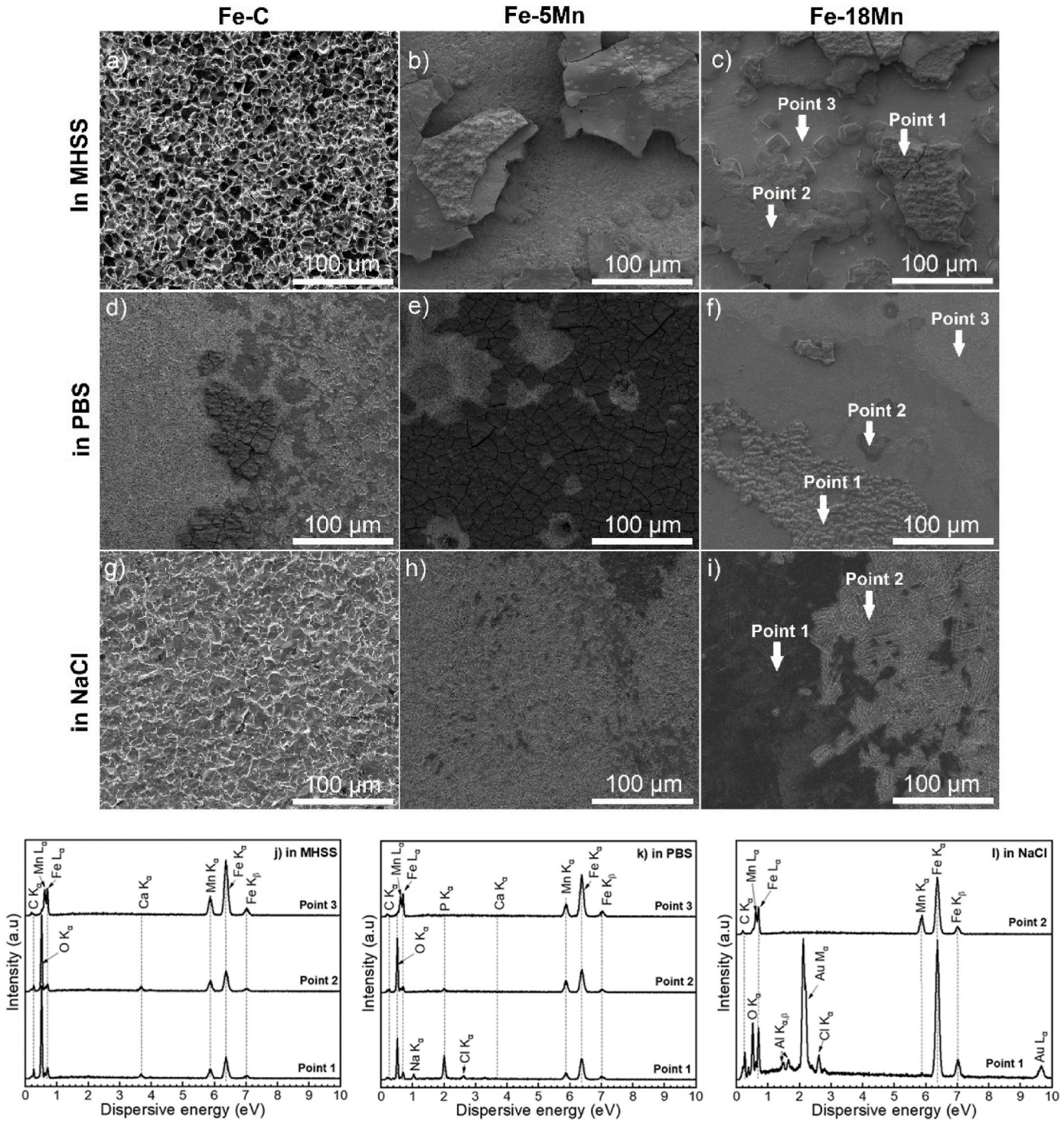

Fig. 4. The degraded surfaces of the three alloys following static immersion degradation tests, along with the EDS analysis results of various DPs-sub-layers on Fe–18Mn degraded surfaces.

analysis confirmed that the inner layer consisted mainly of hydroxides with a minor amount of Cl (Fig. 4l).

The sample surface diffraction patterns after the degradation test are illustrated in Fig. 5; the patterns of the as-received samples are provided for comparison. Despite the presence of degradation layers, and sparse degradation products, no relevant peaks other than those of the substrates were found for all the conditions. $Ca_2P_2O_7$ was identified, consistent with the EDS analysis suggesting that phosphates could form after MHSS exposition. The absence of peaks corresponding to the other possible compounds suggested that the majority of these compounds did not present a crystalline habit. This was also proposed by other authors, for instance, *Huan* et al. [32] found that a dense amorphous layer rich in Zn and oxygen was formed to protect the surface, slow down the degradation rate, and reduce hydrogen evolution per unit time of an Mg–Zn–Zr alloy immersed in Hank's solution.

Fig. 6a–i shows the morphology of the DPs collected from the waste solution after 14 days of static immersion, revealing specific chemical composition for the different media. Those formed in the MHSS solution

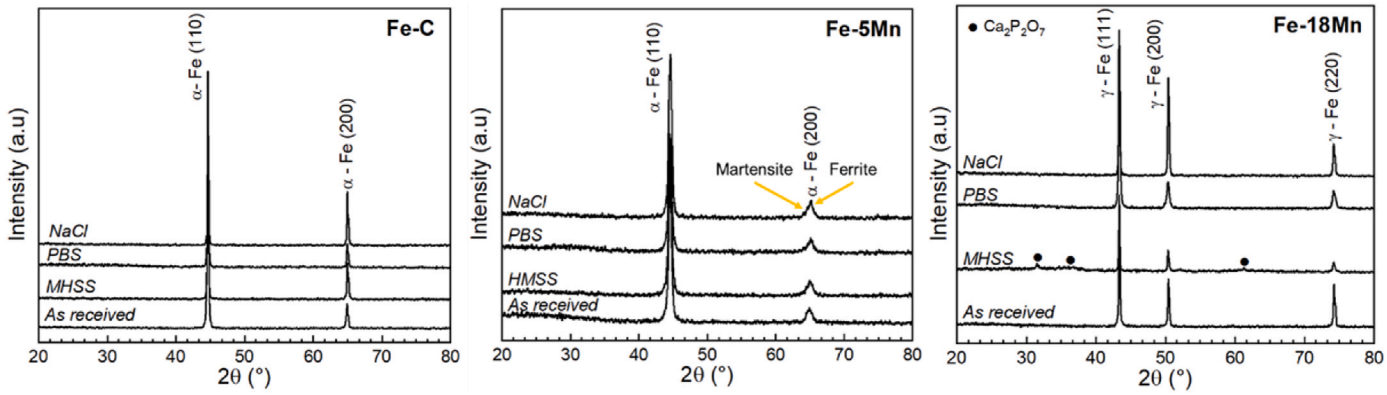

Fig. 5. XRD patterns of the degraded surfaces of Fe–C, Fe–5Mn, and Fe–18Mn alloys after 14 days of static immersion degradation tests in MHSS, PBS, and NaCl. The XRD patterns of Fe–C, Fe–5Mn, and Fe–18Mn as-received samples are reported for comparison.

exhibit a dense structure. Contrary, DPs from the PBS solution are in the form of thin, fragmented plates, and appear to be very stable at the surface, forming a protective layer against further degradation. This may explain the lowest DR observed in PBS. In contrast, degradation in NaCl resulted in DPs with porous structure, facilitating easier solution penetration through the DPs layer and leading to the highest DR.

Fig. 6j-l presents the EDS punctual analysis of the DPs corresponding to the areas indicated by the withe arrows in SEM images in Fig. 6a–i. Regarding the DPs from MHSS (Fig. 6j), P and O were the predominant elements, accompanied by small amounts of Cl, C, Na, and Ca. Hence, the primary constituents of MHSS DPs could be associated mainly to the presence of phosphates, with a minor presence of carbonates, consistent with the EDS analysis from degraded surfaces shown in Fig. 4c. Similarly, PBS DPs exhibited a chemical composition close to that of MHSS, predominantly consistent with the presence of phosphates. The presence of small amounts of carbonates, mixed with phosphates, could also be envisaged, which was consisted with the work of other authors [15]. In contrast, the DPs from NaCl were mainly composed of O, Cl, and Fe, suggesting Cl-containing compounds, and hydroxides as the principal components, as consistent with the existing literature [33].

Fig. 7 shows DPs FTIR spectra. DPs chemical composition was highly dependent on the pseudo-physiological solution used for the immersion tests. For the same medium, FTIR spectra of the three alloys exhibited a similar pattern. In the case of PBS and MHSS DPs peaks related to phosphates (PO_4^{3-}) and to carbonates (CO_3^{2-}) were detected, in the wavenumber ranges of 750–1250 cm^{-1} and 1500–1800 cm^{-1}, respectively. These results confirmed the presence of phosphates as primary DP from PBS and MHSS. Whereas, for NaCl, DPs exhibited instability and solubilized after detachment from the surface, resulting in insufficient powders for FTIR analysis. Finally, a weak peak related to background CO_2 was detected around 2350 cm^{-1} [34].

3.3. Potentiodynamic polarization tests

The potentiodynamic polarization curves were used to understand the electrochemical response of the alloys to polarization. As shown in Fig. 8, all samples behaved similarly in PBS and NaCl. However, in MHSS a noticeable change in electrochemical response was observed, specifically in the anodic region. An active-passive transition behavior for all the alloys occurred around a potential of −0.43 V in the MHSS solution. This could be attributed to the high concentration of aggressive ions, such as SO_4^{2-}, Cl^-, and PO^{3-} (Table 2), which induced localized corrosion. The corresponding kinetic parameters of polarization curves are summarized in Table 4. These results indicate that the polarization also influenced the behavior of alloys and their CRs compared to the static immersion tests. In PBS and NaCl solutions, the CRs remained nearly comparable to those of the immersion tests. Furthermore, current densities increased as the amount of Mn increased from Fe–C, Fe–5Mn to Fe–18Mn, with a high current density for Fe–18Mn reaching 13.9 μA/cm^2 in NaCl solution. Consequently, a consistently high CR was recorded for this medium. In MHSS, the electrochemical analysis revealed distinct trends among the three alloys. The Fe–5Mn alloy exhibited the most active behavior, characterized by the lowest corrosion potential (E_{corr}) and the highest corrosion current density (i_{corr}). In contrast, Fe–C presented the highest E_{corr} and the lowest i_{corr}, reflecting a more passive nature. The electrochemical characteristics of Fe–18Mn fell between those of Fe–C and Fe–5Mn.

As shown in Table 4, the value of the Tafel β_c slope was relatively similar for all alloys, indicating that the reduction reactions occurred according to the same kinetic mechanism.

In contrast, the dissolution of alloys in the MHSS solution exhibits different characteristics, confirmed by significant values of β_α. Moreover, Table 4 indicates that for increasing Mn amounts, there was a consistent shift toward a more cathodic OCP for all the media, which resulted in improved corrosion resistance. Among the three samples, Fe–18Mn shows the most cathodic OCP and, consequently, higher corrosion resistance when compared to Fe–5Mn and Fe–C.

i_{corr} was the highest in the MHSS solution. However, for PBS and NaCl solutions, the electrochemical parameters (E_{corr}, i_{corr}) were very close for each alloy, and all three alloys exhibited low CRs of around 0.098 mm/year in PBS and 0.132 mm/year in NaCl.

Regarding the effect of Mn amount on the polarization behavior of the three alloys, in PBS and NaCl solutions there was no significant influence on the E_{corr} and i_{corr}, thus not affecting the CR. However, in the MHSS solution, all three samples showed an increased CR compared to immersion test results. This could be attributed to the formation of passive layers during immersion tests, which inhibit further degradation. In contrast, during polarization tests, these protective layers were absent, leading to sustained contact between the substrate and the solution and consequently higher CRs. Notably, Fe–5Mn exhibited a five times higher CR than its DR obtained from immersion tests, possibly due to its microstructural characteristics. Fe–5Mn was characterized by a dual-phase microstructure with a small grain size, which likely enhanced its susceptibility to corrosion under polarization conditions.

4. Discussion

4.1. The effect of the testing solutions on the degradation of the three alloys

The degradation behaviors of Fe-based alloys, particularly Fe–Mn alloys, have been extensively investigated by several authors [16,35,36]. Both the current study and previous research suggest that irrespective of Mn content, the DR, properties of passive layers, and resulting DPs are influenced by the chemical composition and ion concentration of the testing solution. For example, in the case of

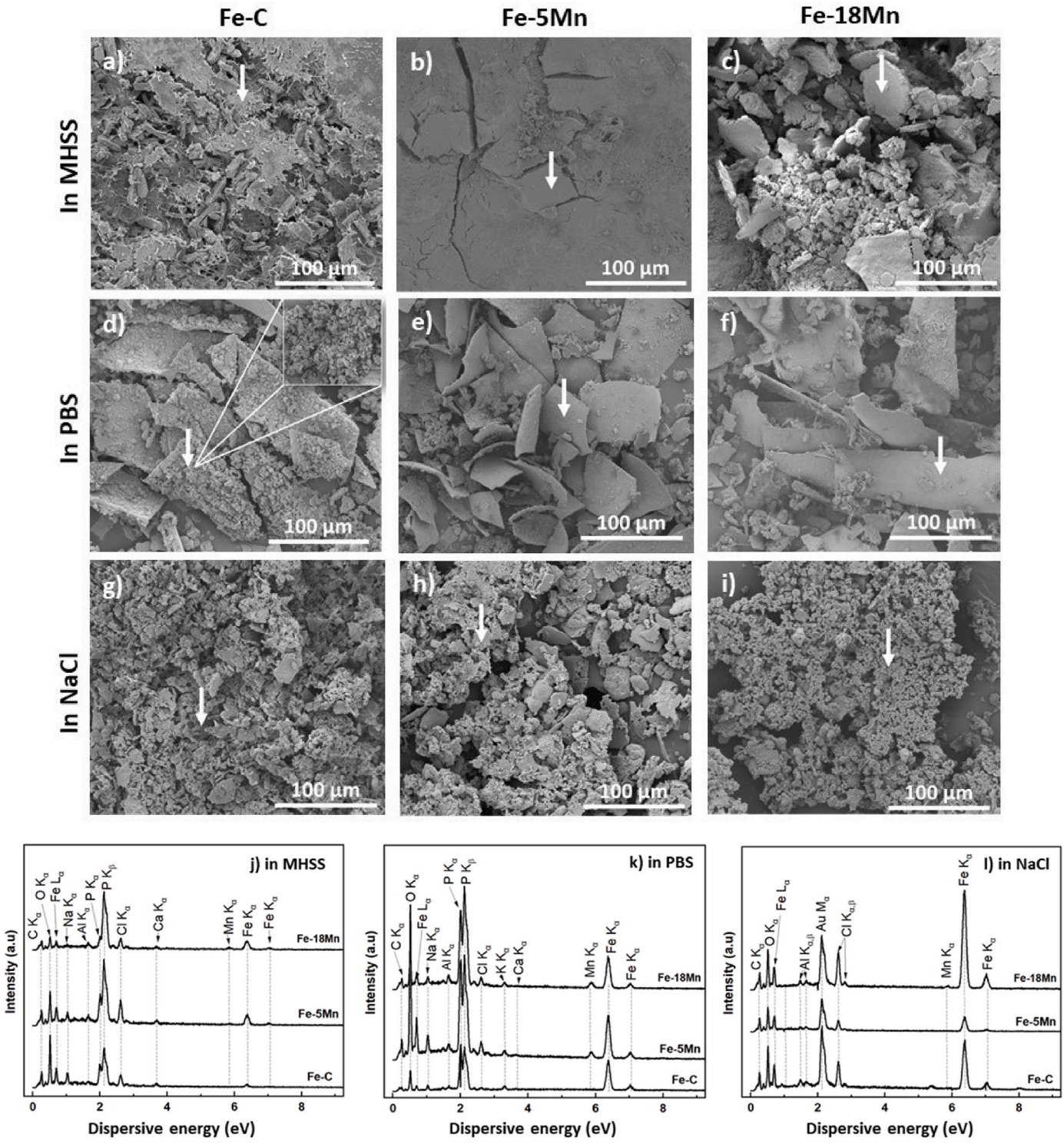

Fig. 6. SEM observation of the DPs collected from waste solutions after static immersion degradation tests for 14 days.

Fe–20Mn-1.2C alloys, *Mouzou* et al. [15] observed that chloride ions (Cl^-) accelerate the DR, while phosphate (PO_4^{3-}) and carbonate (CO_3^{2-}) ions promote the formation of protective passive layers, thus limiting it. Consequently, for the present work, different degradation behaviors were observed across various solutions including MHSS, PBS, and NaCl, leading to distinct DRs and DPs. However, for the same solution, the morphology and chemical composition of degraded surfaces, as well as the resulting DPs, remained largely consistent across all three samples. In this regard, several studies [18,37,38] have reported the general corrosion mechanism of Fe–Mn alloys. This mechanism involves a redox reaction that can be described by the following oxidation and reduction patterns.

- The oxidation of Fe and Mn into Fe^{2+} and Mn^{2+} according to Reaction 1. Moreover, Fe^{2+} may undergo further oxidation to Fe^{3+} (Reaction 2) as reported by *Zhu* et al. [38].

$$M \rightarrow M^{2+}(aq) + 2e^- \quad (1)$$

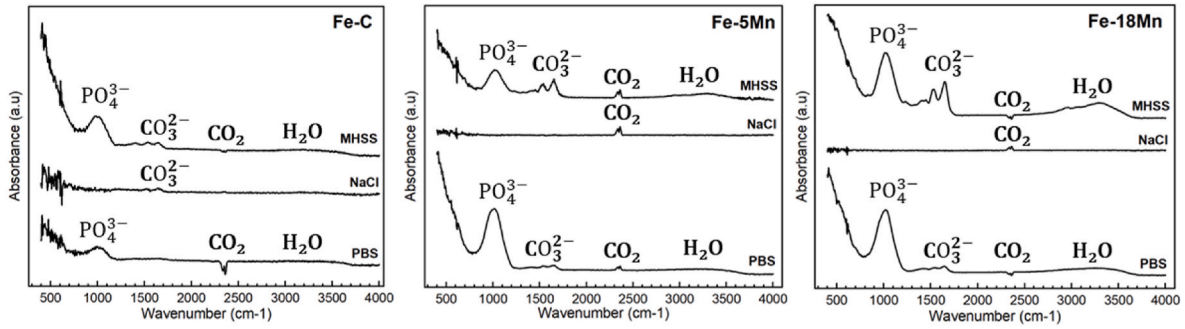

Fig. 7. FTIR spectra of the DPs resulted from the static immersion degradation tests of Fe–C, Fe–5Mn, and Fe-18 Mn alloys in MHSS, PBS, and NaCl solutions.

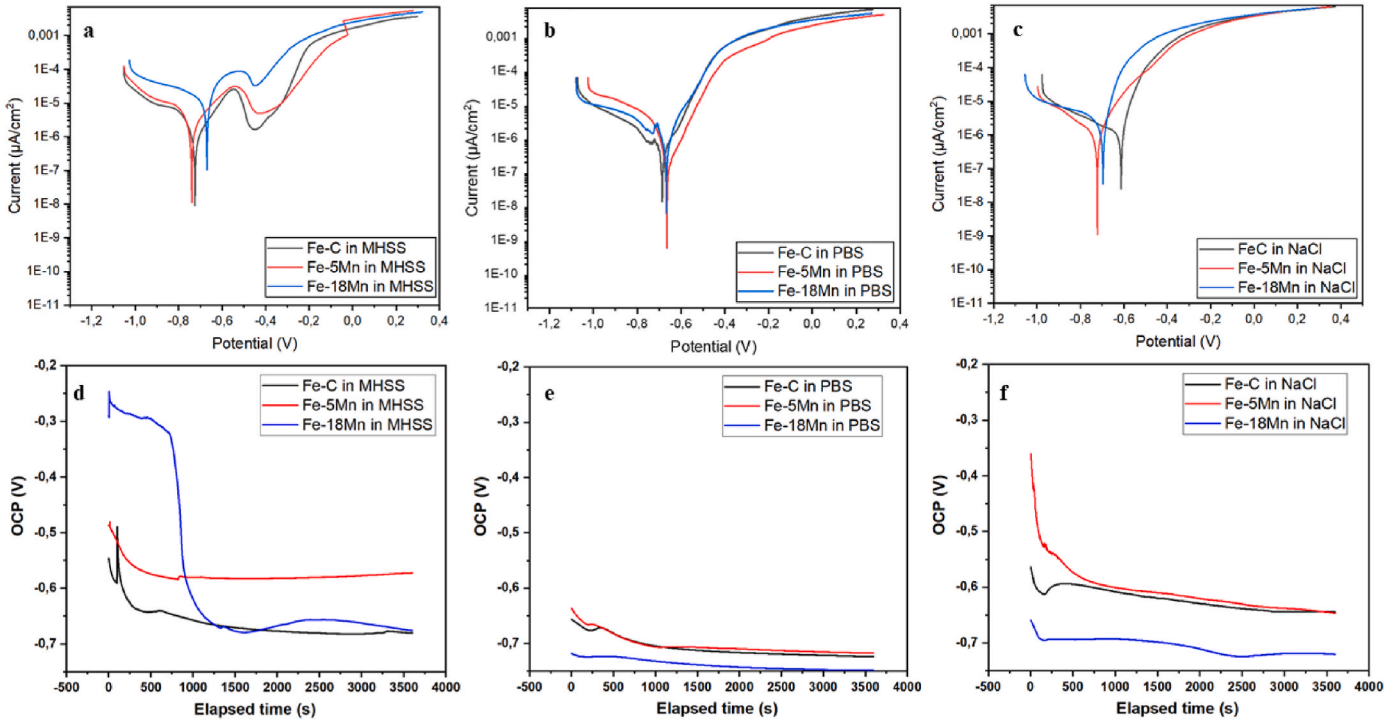

Fig. 8. Potentiodynamic polarization curves for the three alloys in MHSS (a); PBS (b) and NaCl (c). The OCP curves for the three alloys in alloys in MHSS (a); PBS (b) and NaCl (c).

Table 4
Summary of the corrosion data obtained from the PDP tests for the three alloys in MHSS, PBS, and NaCl solution.

Solution	Sample	Electrochemical parameters					
		OCP (V)	E_{corr} (V)	i_{corr} (μA/cm^2)	ß$_a$ (V)	ß$_c$ (V)	CR (mm/year)
MHSS	**Fe–C**	−0.58 ± 0.01	−0.71 ± 0.03	21.96 ± 1.94	0.13 ± 0.01	0.25 ± 0.01	0.26 ± 0.02
	Fe–5Mn	−0.61 ± 0.05	−0.54 ± 0.05	87.55 ± 7.27	0.19 ± 0.03	0.29 ± 0.05	1.02 ± 0.09
	Fe–18Mn	−0.66 ± 0.04	−0.73 ± 0.04	23.65 ± 4.77	0.14 ± 0.01	0.25 ± 0.01	0.28 ± 0.06
PBS	**Fe–C**	−0.71 ± 0.01	−0.67 ± 0.01	6.26 ± 0.99	0.09 ± 0.01	0.26 ± 0.03	0.07 ± 0.01
	Fe–5Mn	−0.71 ± 0.03	−0.67 ± 0.05	7.68 ± 0.45	0.09 ± 0.01	0.19 ± 0.02	0.09 ± 0.01
	Fe–18Mn	−0.75 ± 0.01	−0.72 ± 0.04	11.14 ± 0.71	0.11 ± 0.01	0.27 ± 0.03	0.13 ± 0.01
NaCl	**Fe–C**	−0.64 ± 0.02	−0.71 ± 0.01	9.61 ± 0.26	0.09 ± 0.01	0.29 ± 0.02	0.11 ± 0.01
	Fe–5Mn	−0.64 ± 0.01	−0.71 ± 0.04	10.26 ± 1.39	0.11 ± 0.01	0.25 ± 0.02	0.12 ± 0.02
	Fe–18Mn	−0.72 ± 0.01	−0.73 ± 0.01	13.99 ± 0.29	0.07 ± 0.01	0.33 ± 0.02	0.17 ± 0.01

$Fe^{2+} \rightarrow Fe^{3+}(aq) + e^{-}$ (2)

- The reduction reaction of Fe and Mn in aqueous CO_2-rich environments, which results in the formation of carbonates (Reaction 3) at the interface material-medium.

$M^{2+}(aq) + CO_3^{2-}(aq) \rightarrow MCO_3(aq)$ (3)

Where M refers to Fe or Mn.

4.1.1. *Corrosion mechanism of the three alloys in MHSS*

For MHSS, two distinct layers formed on the surface following static immersion degradation tests as mentioned in paragraph 3.2. EDS results (Fig. 4) could be ascribed to the fact that the inner layer was primarily

composed of hydroxides and carbonates, with Fe, Mn, O, and C as the principal constituents. Carbonate formation could be described by Reaction 3, while hydroxide formation is explained by Reactions 4 and 5.

$$O_2(g) + 2H_2O(l) + 4e^- \rightarrow 4OH^-(aq) \quad (4)$$

$$2Fe^{2+}(aq) + 4OH^-(aq) \rightarrow H_2(g) + 2FeO{\cdot}OH(s) \quad (5)$$

Regarding the top layer, EDS analysis (Fig. 4) revealed the presence of P, O, C, and Ca, attributed to the growth of phosphate layers (Reaction 6) and carbonate precipitates (Reaction 3).

$$3M^{2+}(aq) + 2\ PO_4^{3-}(aq) \rightarrow M_3(PO_4)_2(s) \quad (6)$$

Where M refers to Fe or Mn.

For Fe, two possible reactions may occur, depending on the oxidation state of Fe ions. For Fe^{2+}, the formation of $Fe_3(PO_4)_2$ follows Reaction 6, while for Fe^{3+}, $FePO_4$ is formed according to Reaction 7.

$$Fe^{3+}(aq) + PO_4^{3-} \rightarrow FePO_4(s) \quad (7)$$

SEM images (Fig. 6a–c) showed that the DPs collected from the solution after the static immersion degradation test in MHSS exhibited a dense structure, likely contributing to the observed low DR. In the literature [39,40] it was reported that in MHSS Fe-based alloys DR was initially high before the formation of the observed carbonate/phosphate layers, progressively slowing down as the layer thickness increased. Subsequently, the formation of these DPs on the surface hindered the solution access to the substrate, leading to a delayed DR. EDS (Fig. 6i) and FTIR analysis (Fig. 7) confirmed that the DPs predominantly consisted of phosphates, which agrees with the work conducted by *Loffredo* et al. [18] on Fe–Mn–C alloys, it has been demonstrated that such phosphates remained stable on the surface for up to 28 days of static immersion in Hank's modified solution. In this respect, *Loffredo* et al. [18] carried out long-term static immersion degradation tests for up to 6 months on Fe–16Mn-0.7C alloys using the same conditions as for the current study. They proposed that the degradation process of the investigated alloys within the immersion period took place at 5 main stages: Stage 1 (0–3 days), characterized by a high DR reaching approximately 0.15 mm/year, and no DPs observed for this period; Stage 2 (3–14 days), porous Mn carbonates ($MnCO_3$) layer was formed on the surface leading to a decrease in the DR; Stage 3 (at 28 days), where the porous carbonate layer, initially formed at 14 days, transformed into a nearly compacted layer by day 28 with the precipitation of goethite γ-FeO.OH, which resulted in a reduced DR of below 0.10 mm/year; in Stage 4 (at 60 days), a phosphate layer (Fe, Mn)PO_4 was formed and replaced the previously formed layer made of carbonate, leading to a stoppage of the DR; Stage 5 (120–180 days), where a fully stable and passive two-layer structure emerged, consisting of phosphate and carbonate/hydroxide layers.

4.1.2. Corrosion mechanism of the three alloys in PBS

The PBS solution exhibited the lowest DR in comparison to MHSS and NaCl. This is potentially attributed to the structure of the DP layers formed on the sample surfaces during testing. The examination of SEM images of the degraded surfaces after immersion in PBS (Fig. 4d–f) revealed the formation of two distinct layers. The inner layer primarily consisted of hydroxides, whose formation could be described by Reactions 4 and 5. Additionally, an outer layer of carbonates was observed, thinner and more compact compared to that formed in MHSS, which may be explained by Reaction 3. Moreover, as PBS is characterized by a high concentration of Cl^-, approximately 4947 mg/L (Table 2), traces of Cl-containing phases were detected in the top layer. These compounds likely originated from the reaction of Fe^{2+}, Fe^{3+}, and Mn^{2+} released during the substrate's oxidation reaction (Reactions 1 and 2) with Cl^- present in the solution. In this respect, *Tolouei* et al. [41] investigated the degradation behavior of pure Fe using different pseudo-physiological solutions including PBS. The XRD patterns of the degraded surfaces after 14 days of immersion in PBS revealed the existence of a Cl-containing phase called akaganeite (FeO(OH, Cl)), which is stable in aqueous solutions at 37 °C. The formation of this phase is a complex process and may involve several reactions including the oxidation of Fe^{2+} into Fe^{3+} (Reaction 2), the formation of Fe hydroxide (Reaction 8), and finally the incorporation of Cl^- ions into $Fe(OH)_3$ structure to form akaganeite.

$$Fe^{3+}(aq) + 3OH^-(aq) \rightarrow Fe(OH)_3(s) \quad (8)$$

For PBS, the collected DPs were in the form of thin plates as shown in Fig. 6d–f. These plates were stable preventing further degradation, which may explain the lowest DR obtained for all samples after immersion in PBS solution. The results of the EDS analysis of these DPs presented in Fig. 6k showed that P was the main constituent which suggests that the detached DPs were mainly in the form of phosphates similar to those of MHSS.

4.1.3. Corrosion mechanism of the three alloys in NaCl

Contrary to the exposition to MHSS and PBS, for which the corrosion mechanisms were similar, immersion in NaCl presented a particular pattern. The most relevant aspects could be found from SEM analyses of the degraded surfaces (Fig. 4g–i) after static immersion in NaCl. Here, only some parts of the substrate were covered by a layer of hydroxides and traces of Cl-containing phases after EDS results (Fig. 6l). The outer layer of the DPs was detached completely, which may explain the highest DRs obtained for NaCl as the substrate was exposed to the solution during all 14 days of immersion. Moreover, the detached DPs seem to have a porous structure, then even before their detachment from the surface, the solution was able to penetrate through the porosity and reach the substrate for further degradation.

Fig. 9 illustrates the corrosion mechanisms observed in the three pseudo-physiological solutions for the three alloys. These mechanisms identify the sites of corrosion initiation and describe the final state of the sample surfaces following 14 days of static immersion degradation tests. Notably, monophasic alloys, including the fully ferritic Fe–C and the fully austenitic Fe–18Mn, are grouped in the same mechanism due to their similar degradation behaviors, as described in sections 3.2 and 3.3. In these mechanisms, corrosion starts mainly at the grain boundaries. Conversely, the corrosion mechanism for Fe–5Mn, characterized by a ferrite-martensite microstructure, is distinct. This alloy demonstrates a unique degradation behavior, with corrosion initiation occurring within the ferrite matrix adjacent to martensite laths.

4.2. The effect of Mn content on the alloy degradation in the three solutions

The addition of Mn to Fe is known to be effective in reducing the electrochemical potential by forming a solid solution of Fe and Mn [42]. This can be attributed to the lower electrochemical potential of Mn ($E_0 = -1.185$ V vs SHE) compared to the one of Fe ($E_0 = -0.447$ V vs SHE). Consequently, Fe–Mn alloys exhibit increased degradability in pseudo-physiological solutions in comparison to pure Fe, as supported by several studies [19,43,44]. In the same perspective, alloying Fe matrix with C leads to increased degradation rates for Fe–C alloys when compared with pure Fe [19,45]. Furthermore, the introduction of Fe–Mn–C alloys presented them as promising candidates for biodegradable implants, not only due to their outstanding mechanical properties, but also because of the accelerated degradation facilitated by the synergistic effect of Mn and C as alloying elements [16,18]. For the present study, the selected amounts of C and Mn govern the final microstructure and the phase composition of Fe–Mn–C alloys, as shown in Fig. 1 and Table 3.

The variation in Mn content between Fe–5Mn and Fe–18Mn alloys resulted in distinct matrix microstructures that were exposed to the degradation medium. Fe–5Mn exhibited a dual-phase microstructure

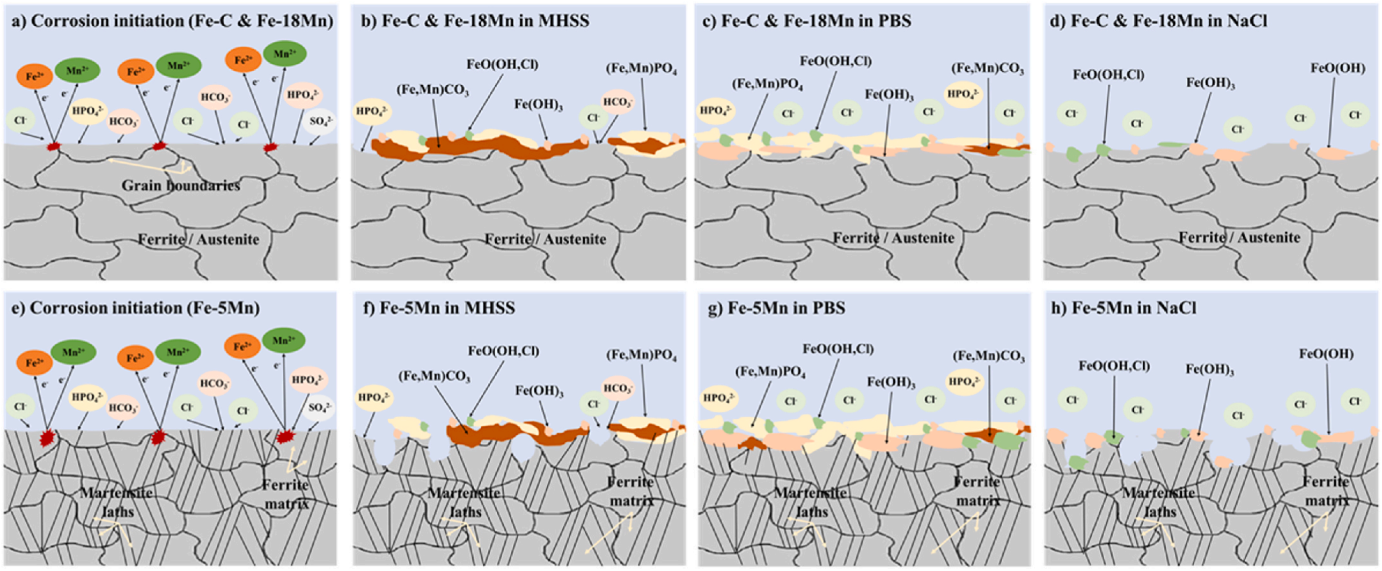

Fig. 9. Corrosion mechanisms of the three alloys in the three pseudo-physiological solutions.

comprising approximately 73 wt% ferrite and 27 wt% martensite, as indicated in Table 3. In contrast, Fe–18Mn showed a fully austenitic microstructure, also documented in Table 3. This difference in microstructure can significantly influence the corrosion susceptibility of the alloys. For instance, the ferrite phase is more vulnerable to corrosion compared to the austenite phase [46]. Notably, the addition of Mn to Fe-based alloys can stabilize the austenite phase by interacting with its crystal lattice structure [47]. Consequently, the higher Mn content in Fe–18Mn promoted a more uniform and stable austenitic phase, enhancing its corrosion resistance compared to Fe–5Mn. This helps explain why Fe–5Mn exhibited higher degradability than Fe–18Mn in the three solutions. Moreover, Fe–5Mn alloy may experience micro-galvanic corrosion cells formed between its ferrite and martensite phases, promoting corrosion compared to the monophasic Fe–18Mn alloy. *Kumar* et al. [48] demonstrated that in dual-phase steels containing ferrite and martensite, the CR depended on the fractions of these phases and the micro-galvanic cells formed between them. Specifically, they showed that in cases like Fe–5Mn, ferrite acts as micro-anodic sites while martensite serves as micro-cathodic ones, increasing corrosion.

Furthermore, it is well-established that higher amounts of grain boundaries in Fe–Mn alloys correlate with increased DRs [49]. These boundaries serve as sites for corrosion initiation. For instance, *Schinhammer* et al. [50] demonstrated that in a pseudo-physiological solution, the twin boundaries of the Fe–21Mn-0.7C–1Pd alloy serve as privileged sites for degradation initiation. Additionally, it has been observed that due to inherent distortion in grain boundaries, corrosion predominantly originates from the adjacent Fe matrix when exposed to physiological solutions such as SBF and Hanks' modified [51]. In this regard, Fe–5Mn exhibited a fine microstructure with an average grain size of approximately 8 μm, resulting in a high concentration of grain boundaries. This contributed to the high DR observed for Fe–5Mn compared to Fe–18Mn. However, the phase composition exerted a greater influence on the alloy degradation than grain size (grain boundary density). This was evident for Fe–C and Fe–5Mn DRs. Despite both alloys having similar grain sizes (around 6 μm for Fe–C and 8 μm for Fe–5Mn alloy, as shown in Table 3, the dual-phase microstructure of Fe–5Mn alloy led to significantly higher degradation compared to the monophasic microstructure of Fe–C alloy.

In MHSS and NaCl, Fe–C and Fe–18Mn showed comparable DRs, suggesting a complex interaction between various degradation-influencing factors. On one hand, the Fe–18Mn alloy, with its higher Mn content (18 wt%), exhibited a reduced standard potential compared to the Fe–C alloy. This was evident in the lower OCP observed for Fe–18Mn compared to Fe–C (Fig. 8), indicating a higher susceptibility to corrosion for Fe–18Mn. On the other hand, Fe–C exhibited a fully ferritic microstructure with a fine grain size of approximately 6 μm, while Fe–18Mn had an austenitic microstructure with larger grains of about 20 μm. Consequently, Fe–C was anticipated to degrade more rapidly than Fe–18Mn based on these microstructural factors. In the end, it appears that the combined impact of these factors led to similar DRs for Fe–18Mn and Fe–C alloys in the two solutions. In the case of the PBS solution, the influence of Mn was attenuated by the development of a phosphate layer on the sample surfaces during degradation. This resulted in very low and comparable DRs for all three alloys.

5. Conclusion

This work investigated the degradation behavior of Fe-based alloys with varying Mn and C contents in three different pseudo-physiological solutions. The key findings can be summarized as follows.

- Fe–5Mn-0.2C alloy, characterized by a mixture of ferrite and martensite with an average grain size of 8 μm, exhibited the highest DR for all three solutions.
- Fe-0.15C alloy, characterized by a fully ferritic microstructure with a fine grain size of 6 μm, demonstrated degradation behavior and rates similar to those of Fe–18Mn-0.6C alloy, which had a fully austenitic microstructure with larger grains (20 μm).
- Phosphates and carbonates were identified as the primary DPs in MHSS and PBS solutions. These products formed a protective solid layer, reducing further corrosion of the substrates and resulting in lower DRs.
- Chlorine-containing compounds (such as akaganeite FeO(OH,Cl)) were DP species, present especially after NaCl exposure. These compounds exhibited a porous structure, facilitating solution penetration. Moreover, they showed lower stability on the surface, which led to their detachment into the solution during testing. This allowed continuous contact between the solution and substrate, consequently resulting in the highest DR observed among the three solutions.

While this research systematically explored the short-term (14 days) degradation behavior of Fe-based alloys in various pseudo-physiological solutions, longer immersion tests are recommended to comprehensively understand the long-term degradation behavior of these alloys for

practical applications.

Ethics approval and consent to participate

This study did not involve human subjects, patients, or animals. As a result, there were no ethical considerations related to the participation of individuals in the research. Therefore, ethical approval and consent to participate were not applicable.

CRediT authorship contribution statement

Abdelhakim Cherqaoui: Writing – review & editing, Writing – original draft, Methodology, Investigation. **Quang Nguyen Cao:** Writing – review & editing, Writing – original draft, Methodology, Investigation, Conceptualization. **Maria Laura Gatto:** Writing – original draft. **Carlo Paternoster:** Writing – review & editing, Writing – original draft, Validation, Conceptualization. **Paolo Mengucci:** Methodology, Investigation. **Diego Mantovani:** Writing – review & editing, Validation, Supervision, Conceptualization.

Declaration of competing interest

Prof. Diego Mantovani is an associate editor and guest editor for Bioactive Materials Special issue 15th Biometal, he was not involved in the editorial review or the decision to publish this article. All authors declare that there are no competing interests.

Acknowledgements

This work was mainly supported by the Natural Science and Engineering Research Council of Canada, and PRIMA (Quebec Ministry for Economy and Innovation). DM holds a Canada Research Chair Tier I (2012–2026).

References

[1] T. Kraus, et al., Biodegradable Fe-based alloys for use in osteosynthesis: Outcome of an in vivo study after 52 weeks, Acta Biomater. 10 (7) (2014) 3346–3353.
[2] M. Schinhammer, et al., Recrystallization behavior, microstructure evolution and mechanical properties of biodegradable Fe–Mn–C (–Pd) TWIP alloys, Acta Mater. 60 (6–7) (2012) 2746–2756.
[3] F. Moszner, et al., Atomic-scale characterization of prior austenite grain boundaries in Fe–Mn-based maraging steel using site-specific atom probe tomography, Acta Mater. 73 (2014) 215–226.
[4] V.M. Rabeeh, T. Hanas, Progress in manufacturing and processing of degradable Fe-based implants: a review, Progress in biomaterials 11 (2) (2022) 163–191.
[5] M. Peuster, et al., Long-term biocompatibility of a corrodible peripheral iron stent in the porcine descending aorta, Biomaterials 27 (28) (2006) 4955–4962.
[6] K. Ueki, R. Hirano, M. Nakai, Development of biodegradable Fe-Mn-Mg alloys by mechanical alloying and spark plasma sintering, Mater. Today Commun. 34 (2023) 105465.
[7] P. Goudarzi, M. Moazami-Goudarzi, A. Masoudi, Sintering, microstructure and properties of absorbable Fe–Mn-xCu alloys, Mater. Chem. Phys. 287 (2022) 126368.
[8] L. Saliba, et al., FeMn and FeMnAg biodegradable alloys: an in vitro and in vivo investigation, Helion 9 (5) (2023).
[9] B. Wegener, et al., Development of a novel biodegradable porous iron-based implant for bone replacement, Sci. Rep. 10 (1) (2020) 9141.
[10] M.S. Dargusch, et al., Exploring the role of manganese on the microstructure, mechanical properties, biodegradability, and biocompatibility of porous iron-based scaffolds, ACS Biomater. Sci. Eng. 5 (4) (2019) 1686–1702.
[11] A. Bartkowska, et al., Biodegradable porous FeMn (–x Ag) alloys: assessment of cytocompatibility, mechanical, magnetic and antibiofilm properties, Materials Advances 4 (2) (2023) 616–630.
[12] B. Paul, et al., Effect of Blasting treatments on the surface Topography and cell Adhesion on biodegradable FeMn-based stents processed by Laser powder bed Fusion, Adv. Eng. Mater. 24 (10) (2022) 2200961.
[13] P. Liu, et al., Microstructure, mechanical properties and corrosion behavior of additively-manufactured Fe–Mn alloys, Mater. Sci. Eng. 852 (2022) 143585.
[14] D. Carluccio, et al., Additively manufactured iron-manganese for biodegradable porous load-bearing bone scaffold applications, Acta Biomater. 103 (2020) 346–360.
[15] E. Mouzou, et al., In vitro degradation behavior of Fe–20Mn–1.2 C alloy in three different pseudo-physiological solutions, Mater. Sci. Eng. C 61 (2016) 564–573.
[16] S. Gambaro, et al., Mechanical and degradation behavior of three Fe-Mn-C alloys for potential biomedical applications, Mater. Today Commun. 27 (2021) 102250.
[17] M.C. Conti, et al., Influence of cold rolling on in vitro cytotoxicity and electrochemical behaviour of an Fe-Mn-C biodegradable alloy in physiological solutions, Helion 4 (11) (2018).
[18] S. Loffredo, et al., Six-month long in vitro degradation tests of biodegradable twinning-induced plasticity steels alloyed with Ag for stent applications, ACS Biomater. Sci. Eng. 7 (8) (2021) 3669–3682.
[19] B. Liu, Y. Zheng, Effects of alloying elements (Mn, Co, Al, W, Sn, B, C and S) on biodegradability and in vitro biocompatibility of pure iron, Acta Biomater. 7 (3) (2011) 1407–1420.
[20] H. Schumann, Martensitische Umwandlungen in Austenitischen Mangan-Kohlenstoff-Stählen, 1972.
[21] T. Peters, All about Albumin: Biochemistry, Genetics, and Medical Applications, Academic press, 1995.
[22] G. Vander Voort, *Is there possible Bias in ASTM E112 Planimetric grain size measurements?* Materials performance and characterization 2 (1) (2013) 194–205.
[23] A. Nace, ASTM G31-12a: Standard Guide for Laboratory Immersion Corrosion Testing of Metals vol. 100, ASTM International, 2012, p. 19428, 2959.
[24] G. Astm, Standard test method for conducting potentiodynamic polarization resistance measurements, Annu. Book ASTM (Am. Soc. Test. Mater.) Stand. 3 (2009) 237–239.
[25] S. Loffredo, et al., Effect of silver on corrosion behavior of plastically deformed twinning-induced plasticity steel for biodegradable stents, JOM 72 (2020) 1892–1901.
[26] M. Koyama, et al., Microstructure and plasticity evolution during Lüders deformation in an Fe-5Mn-0.1 C medium-Mn steel, ISIJ Int. 62 (10) (2022) 2036–2042.
[27] K. Steineder, et al., On the microstructural characteristics influencing the yielding behavior of ultra-fine grained medium-Mn steels, Acta Mater. 139 (2017) 39–50.
[28] A. Knaislová, et al., Critical assessment of techniques for the description of the phase composition of advanced high-strength steels, Materials 12 (24) (2019) 4033.
[29] L. Xiao, et al., Lattice-parameter variation with carbon content of martensite. I. X-ray-diffraction experimental study, Phys. Rev. B 52 (14) (1995) 9970.
[30] J.T. Benzing, et al., Multi-scale characterization of austenite reversion and martensite recovery in a cold-rolled medium-Mn steel, Acta Mater. 166 (2019) 512–530.
[31] G. Mishra, A. Chandan, S. Kundu, Hot rolled and cold rolled medium manganese steel: mechanical properties and microstructure, Mater. Sci. Eng. 701 (2017) 319–327.
[32] Z. Huan, et al., In vitro degradation behavior and cytocompatibility of Mg–Zn–Zr alloys, J. Mater. Sci. Mater. Med. 21 (2010) 2623–2635.
[33] J. Venezuela, M. Dargusch, Addressing the slow corrosion rate of biodegradable Fe-Mn: current approaches and future trends, Curr. Opin. Solid State Mater. Sci. 24 (3) (2020) 100822.
[34] G. González-Gaitano, J.R. Isasi, Analysis of the rotational structure of CO2 by FTIR spectroscopy, Chem. Educat. 6 (6) (2001) 362–364.
[35] P. Liu, et al., Microstructure, mechanical properties, degradation behavior, and biocompatibility of porous Fe-Mn alloys fabricated by sponge impregnation and sintering techniques, Acta Biomater. 114 (2020) 485–496.
[36] S. Wei, et al., Effect of copper content on the biodegradation behavior of Fe-Mn-C alloy system, Mater. Technol. 37 (9) (2022) 1109–1119.
[37] H. Hermawan, et al., Fe–Mn alloys for metallic biodegradable stents: degradation and cell viability studies, Acta Biomater. 6 (5) (2010) 1852–1860.
[38] S. Zhu, et al., Biocompatibility of pure iron: in vitro assessment of degradation kinetics and cytotoxicity on endothelial cells, Mater. Sci. Eng. C 29 (5) (2009) 1589–1592.
[39] C. Tonna, et al., Biodegradation behaviour of Fe-based alloys in Hanks' Balanced Salt Solutions: Part I. material characterisation and corrosion testing, Bioact. Mater. 7 (2022) 426–440.
[40] A. Drynda, et al., In vitro and in vivo corrosion properties of new iron–manganese alloys designed for cardiovascular applications, J. Biomed. Mater. Res. B Appl. Biomater. 103 (3) (2015) 649–660.
[41] R. Tolouei, et al., The use of multiple pseudo-physiological solutions to simulate the degradation behavior of pure iron as a metallic resorbable implant: a surface-characterization study, Phys. Chem. Chem. Phys. 18 (29) (2016) 19637–19646.
[42] Y.F. Zheng, X.N. Gu, F. Witte, Biodegradable metals, Mater. Sci. Eng. R Rep. 77 (2014) 1–34.
[43] M. Schinhammer, et al., Design strategy for biodegradable Fe-based alloys for medical applications, Acta Biomater. 6 (5) (2010) 1705–1713.
[44] H. Hermawan, D. Dubé, D. Mantovani, Degradable metallic biomaterials: design and development of Fe–Mn alloys for stents, J. Biomed. Mater. Res. Part A: An Official Journal of The Society for Biomaterials, The Japanese Society for Biomaterials, and The Australian Society for Biomaterials and the Korean Society for Biomaterials 93 (1) (2010) 1–11.
[45] C. Shuai, et al., Strong corrosion induced by carbon nanotubes to accelerate Fe biodegradation, Mater. Sci. Eng. C 104 (2019) 109935.
[46] J.-S. Lee, et al., Corrosion behaviour of ferrite and austenite phases on super duplex stainless steel in a modified green-death solution, Corrosion Sci. 89 (2014) 111–117.
[47] J. Zhou, et al., Relationship between austenite-Stabilizing elements and austenite fraction in Near-rapidly Solidified Fe–Mn–Al–C Lightweight steel, Steel Res. Int. 93 (11) (2022) 2200422.

[48] S. Kumar, et al., Mechanical and electrochemical behavior of dual-phase steels having varying ferrite–martensite volume fractions, J. Mater. Eng. Perform. 28 (2019) 3600–3613.
[49] J. Hufenbach, et al., Novel biodegradable Fe-Mn-CS alloy with superior mechanical and corrosion properties, Mater. Lett. 186 (2017) 330–333.
[50] M. Schinhammer, et al., Degradation performance of biodegradable Fe-Mn-C(-Pd) alloys, Mater. Sci. Eng., C 33 (4) (2013) 1882–1893.
[51] J. Deng, et al., Large lattice mismatch effects on the epitaxial growth and magnetic properties of FePt films, J. Magn. Magn Mater. 446 (2018) 125–134.